Magnetic Resonance Imaging 63 (2019) 193–204

Contents lists available at ScienceDirect

Magnetic Resonance Imaging

journal homepage: www.elsevier.com/locate/mri

Original contribution

High resolution time-of-flight MR-angiography at 7 T exploiting VERSE saturation, compressed sensing and segmentation

Christian R. Meixner[a,*], Patrick Liebig[b,c], Peter Speier[b], Christoph Forman[b], Bernhard Hensel[c], Manuel Schmidt[d], Marc Saake[a], Michael Uder[a], Arnd Doerfler[d], Robin M. Heidemann[b], Sebastian Schmitter[e,f], Armin M. Nagel[a,f,g]

[a] Institute of Radiology, University Hospital Erlangen, Friedrich-Alexander Universität Erlangen-Nürnberg (FAU), Erlangen, Germany
[b] Siemens Healthcare GmbH, Erlangen, Germany
[c] Max Schaldach-Stiftungsprofessur für Biomedizinische Technik (MSBT), Friedrich-Alexander Universität Erlangen-Nürnberg (FAU), Erlangen, Germany
[d] Department of Neuroradiology, University Hospital Erlangen, Friedrich-Alexander Universität Erlangen-Nürnberg (FAU), Erlangen, Germany
[e] Physikalisch-Technische Bundesanstalt, Berlin, Germany
[f] Division of Medical Physics in Radiology, German Cancer Research Center (DKFZ), Heidelberg, Germany
[g] Institute of Medical Physics, Friedrich-Alexander Universität Erlangen-Nürnberg (FAU), Erlangen, Germany

ARTICLE INFO

Keywords:
Time-of-flight
MR-angiography
Compressed sensing
7 Tesla
VERSE
Ultra-high field

ABSTRACT

Background: 3D Time-of-Flight (TOF) MR-angiography (MRA) substantially benefits from ultra-high magnetic field strengths (≥7 T) due to increased Signal-to-Noise ratio and improved contrast. However, high-resolution TOF-MRA usually requires long acquisition times. In addition, specific absorption rate constraints limit the choice of optimal pulse sequence parameters, especially if venous saturation is employed.

Purpose: To implement and evaluate an arterial TOF-MRA for accelerated high-resolution angiography at ultra-high magnetic field strength.

Field strengths/sequence: 7 T modified gradient-echo TOF sequence including venous saturation using Variable-Rate Selective Excitation (VERSE), Compressed Sensing (CS) and sparse application of saturation pulses, called segmentation, were included for acceleration.

Assessment: To analyze the acceleration techniques all volunteers were examined with the same protocols. CS with different sampling patterns and regularization factors as well as segmentation were applied for acceleration. For comparison, conventional acceleration techniques were applied (GRAPPA PAT 3 and Partial Fourier (6/8 in slice/phase encoding)). Images were co-registered and 40 mm thick transversal maximum intensity projections were created to calculate the relative number of vessels. To analyze the visibility of small vessels, the lenticulostriate arteries (LSA) were examined. This was done via multiscale vessel enhancement filtering in a VOI and quantification via Fiji ImageJ as well as qualitatively evaluation by two radiologists. Additionally, the venous/arterial vessel-to-background ratios (vVBR/aVBR) were calculated for chosen protocols.

Results: For the acceleration of a high resolution TOF-MRA (0.31 mm isotropic), under-sampling of 9.6 showed aliasing artifacts, whereas 7.2 showed no aliasing. The regularization factor R had a strong impact on the image quality according to smoothing ($R = 0.01$ to $R = 0.005$) and noise ($R = 0.0005$ to $R = 0.00005$). With the alternating sampling patterns it was shown that the k-space center should not be under-sampled too much.

Abbreviations: aVBR, arterial vessel-to-background ratio; CE-MRA, contrast enhanced MRA; Conv, conventional acceleration; CS, Compressed Sensing; $CS_{7.2,\ 71\%}$, CS with acceleration factor 7.2, Poisson disk radius 71%; $CS_{7.2,\ 80\%}$, CS with acceleration factor 7.2, Poisson disk radius 80%; $CS_{7.2,\ 80\%,\ 3\ Seg}$, CS with acceleration factor 7.2, Poisson disk radius 80%, 3 Segments; $CS_{7.2,\ 80\%,\ 3\ Seg,\ TR2 < TR1}$, CS with acceleration factor 7.2, Poisson disk radius 80%, 3 Segments, $TR_2 < TR_1$; $CS_{7.2,\ 90\%}$, CS with acceleration factor 7.2, Poisson disk radius 90%; $CS_{9.6,\ 80\%}$, CS with acceleration factor 9.6, Poisson disk radius 80%; DSA, digital subtraction angiography; FOV, field-of-view; GRAPPA, Generalized Auto-calibrating Partial Parallel Acquisition; mFISTA, Modified Fast Iterative Shrinkage-Thresholding Algorithm; MIP, maximum intensity projection; MRA, magnetic resonance angiography; PI, parallel imaging; SAR, specific absorption rate; SENSE, Sensitivity Encoding; SNR, signal-to-noise ratio; SSS, superior sagittal sinus; TA, acquisition time; TOF, Time-of-Flight; TR, repetition time; $\overline{TR}$, mean repetition time; UHF, ultra-high magnetic field; VERSE, Variable-Rate Selective Excitation; VOI, volume of interest; vVBR, venous vessel-to-background ratio

* Corresponding author at: Institute of Radiology, University Hospital Erlangen, Friedrich-Alexander Universität Erlangen-Nürnberg (FAU), Maximiliansplatz 3, 91054 Erlangen, Germany.
E-mail address: christian.meixner@uk-erlangen.de (C.R. Meixner).

https://doi.org/10.1016/j.mri.2019.08.014
Received 5 March 2019; Received in revised form 4 August 2019; Accepted 15 August 2019

Additionally segmentation could be verified to be feasible for stronger acceleration with sufficient venous suppression.

Conclusion: The combination of several independent techniques (VERSE, CS with acceleration factor 7.2, $R = 0.001$, Poisson disc radius of 80%, 3 segments) enables the application of high-resolution (0.31 mm isotropic) TOF-MRA with venous saturation at 7 T in clinical time settings (TA ≈ 5 min) and within the SAR limits.

1. Introduction

Time-of-Flight (TOF) magnetic resonance angiography (MRA) enables non-invasive visualization of blood vessel without intravenous contrast agent. Thus, also patients for whom the use of contrast agents is contraindicated (e.g. due to renal insufficiency [1]) can be examined. In addition, some MRA examinations in the brain cannot be performed on T1-weighted contrast-enhanced images, due to a break-down of the blood-brain barrier. For example, non-specific contrast media extravasation prevents visualization of small tumor vessels in glioblastomas [2]. Thus, the target of this study is MRA in the human brain; there TOF-MRA has been already successfully applied for the detection of cerebral vasculitis, aneurysms, arteriosclerosis or arteriovenous malformation [3–5]. However, digital subtraction angiography (DSA) is still the gold standard for the depiction of vessels in the human brain, especially if high resolution imaging (< 0.5 mm) is required. Nevertheless, in many cases the contrast-enhanced DSA can be replaced by MRA [3,4]. This is important with regard to radiation exposure and enables the inclusion of MRA protocols in MRI examinations. Likewise, vessels that are directly attached to the bone are less visible in DSA [1]. In today's clinical setting, TOF-MRA, used at 1.5 or 3 T, suffers from low spatial resolution (> 0.5 mm) or long acquisition times (TA) (> 10 min) [5,6]. The depiction of small vessels, such as the lenticulostriate arteries (LSA) [7,8], would amongst others be highly desirable for example when examining the vascular component of neurodegenerative diseases such as Alzheimer's disease, Parkinson, multiple sclerosis, migraine and depression [5,9–11].

TOF-MRA benefits multifold from ultra-high magnetic field (UHF) strengths ($B_0 \geq 7$ T) [12]. UHF MRI results in increased signal-to-noise ratio (SNR) [13,14] and prolonged T1 constants of brain tissue [15,16], which enable higher spatial resolution (< 0.5 mm) and result in improved image contrast, respectively.

However, higher spatial resolution in general leads to longer acquisition times if the same field-of-view (FOV) is sampled [17]. Parallel imaging (PI) techniques such as Generalized Auto-calibrating Partial Parallel Acquisition (GRAPPA) [18] or Sensitivity Encoding (SENSE) [19] as well as Partial Fourier can accelerate image acquisitions. Several publications of high resolution protocols (< 0.5 mm) [7,17,20–22] show the need of additional acceleration, due to acquisition times of approximately 8 to 33 min for the same covering as intended in this work. Long acquisition times increase the likelihood of patient movement, making high-resolution imaging prone to motion artifacts [17] and - without motion correction - higher acceleration essential. It has already been demonstrated at 7 T, that with the help of Compressed Sensing (CS) the acquisition time for TOF imaging can be shortened without loss of image quality [8,23,24]. In these works, relatively small acceleration factors (3.2–5) were applied, which is still lower than at 3 T, where 6-fold acceleration is already feasible [25]. According to the higher SNR and larger matrix sizes at 7 T, larger acceleration factors than at 3 T [26] should be possible.

With increasing field strength also the specific absorption rate (SAR) increases [27]. Thus, energy-intensive pulses for venous saturation limit the choice of optimal parameter settings due to SAR limitations [28]. As a result, TOF-sequences at 7 T are usually performed with sub-optimal parameters only, such as longer TR, smaller flip angle as desirable or without saturation pulses. This can lead to sub-optimal image contrast, long acquisition times or only partly suppressed venous signal [5,15]. In previous works, lower flip angles for saturation pulses [21], segmentation and corresponding sparse application of venous saturation pulses [29] or Variable-Rate Selective Excitation (VERSE) pulses [28] were used to overcome this limitation. However, lower flip angles lead to an increasing venous vessel-to-background ratio (vVBR) and therefore poor venous saturation [21,29].

In this work, a scan time and contrast optimized high resolution protocol for small vessel TOF-MRA (0.31 mm isotropic voxel size) in the human brain was developed. In contrast to earlier works [8,23,24] the sequence provides, beside prospective CS and parallel imaging [30–32], venous saturation under SAR constraints [28], segmented saturation (from now on called “segmentation”) [29] and online reconstruction to achieve high-resolution TOF-MRA images. The venous and fat saturation were achieved using VERSE saturation pulses [28]. Due to the high sensitivity of VERSE to off-resonance it was not used for excitation. At the same time, this effect was used for fat saturation in the FOV via the VERSE saturation pulses [28]. The performance of the sequence was evaluated by examinations of healthy subjects. In particular, qualitative analyses were performed by two radiologists and quantitative evaluations were performed using two metrics – one tailored to all detected vessels, one to small vessels.

2. Material and methods

All measurements were performed on a 7 T MR system (MAGNETOM Terra, Siemens Healthcare GmbH, Erlangen, Germany) using a 32-channel Rx/1Tx head-coil (Nova Medical, Wilmington, Massachusetts, USA). Ten healthy volunteers were included (mean age: 24.3 ± 3.5). All measurements were carried out in accordance with the institutional guidelines and with approval of the local Ethics Committee (Friedrich-Alexander University (FAU) Erlangen-Nürnberg, Germany).

2.1. Data acquisition

2.1.1. Used sequence

A 3D-gradient echo TOF sequence was modified to perform venous saturation using VERSE pulses (Fig. 1). Therefore, an algorithm as proposed by Schmitter et al. [28], which is based on the work of Conolly et al. [33], was implemented. For all measurements the RF-amplitude for the venous saturation pulses was reduced to 25% compared to the original provided Sinc pulse, while the duration was kept constant: 3584 µs (Fig. 1). It was taken advantage of the off-resonance sensitivity of the VERSE pulses to achieve fat saturation in the image layer [28]. Therefore, the distance of the saturation layer and the FOV was 17 mm and the thickness of the saturation layer was 40 mm. VERSE pulses for venous saturation is used for all sequences in this work, while for excitation, asymmetric Sinc pulses (1536 µs) were applied. Regarding SAR, all scans were performed within the first level mode of the regulations of the International Electrotechnical Commission [34]. Therefore, SAR values are presented normalized to the limit of the first level mode provided by the scanner. Consequently, a value of 50% equals the limit of the normal level mode.

The sparse acquisition of the k-space data was performed in form of a highly under-sampled variable-density Poisson disk with a Gaussian density distribution (Fig. 2a) [35,36]. The radius of the Poisson disk is given as a percentage relative to the length of the diagonal in the phase encoding planes. As a special case, 71% correspond to elliptical scanning. 32 reference scans for the auto-calibration of the coil sensitivity maps were placed in the k-space center (Fig. 2b). In the two phase-

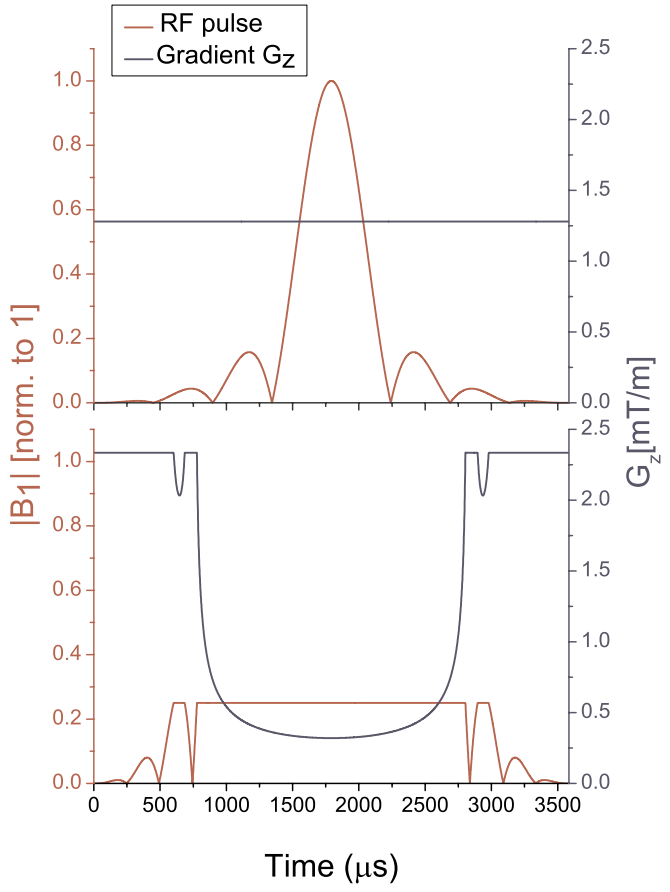

Fig. 1. RF saturation pulses, normalized to 1 with slice selection Gradient G_z: Top: Original Sinc pulse of the saturation with a duration of 3584 µs and constant gradient. Bottom: Modified saturation pulse and gradient using VERSE. An amplitude reduction factor of 25% was applied. The pulse duration was kept constant.

encoding directions, linear reordering from red over gray to blue was applied. The frequency encoding direction (anterior – posterior) was fully sampled.

To enable additional acceleration, segmentation was applied. Thereby, one saturation pulse followed several excitation pulses [29]. As shown by Zhang et al. [29] the deviation of the signal intensity of the different k-space points resulting from two different repetition times (TR_1 and TR_2) is averaged over the entire k-space, so that an average TR ($\overline{TR}$) can be calculated:

$$\overline{TR} = \frac{TR}{number\ of\ segments} = \frac{TR_1 + (number\ of\ segments - 1) \cdot TR_2}{number\ of\ segments} \quad (1)$$

Also with segmentation, the data has been sampled in linear reordering, as there is no favorable filling scheme for segmented TOF protocols as shown in [29].

2.1.2. Measured and evaluated protocols

The initial protocol was an optimized sequence for high-resolution imaging at 7 T with a resolution of $(0.31\ mm)^3$, a field of view (FOV) of 220x174x59 mm^3 and a distance factor of −19.64% at 4 slabs à 56 slices with 14.3% oversampling in slice direction. Additional Tilt-Optimized Nonsaturated Excitation (TONE) pulses [37] with a TONE ramp of 70% were used for excitation. As a gold standard in clinical routine, conventional acceleration (GRAPPA, Partial Fourier 6/8 in slice and phase encoding direction) (Conv) was used for the initial protocol as well as VERSE pulses for venous saturation as described before (RF amplitude was reduced to 25%, duration: 3584 µs; compare Fig. 1). With these conventional acceleration techniques (GRAPPA and Partial Fourier) the protocol could be accelerated by a factor of 3.7. VERSE saturation is required to decrease SAR below the limits of the first level mode (i.e. < 100%). Conventional saturation using Sinc pulses would result in relative SAR values of 193.4 ± 20.3%, which means that the protocol could not be applied with the given parameters.

Subsequently, the sequence was tested with different CS accelerations ($CS_{9.6,\ 80\%}$: acceleration factor 9.6, Poisson disk radius 80%, $CS_{7.2,\ 80\%}$: acceleration factor 7.2, Poisson disk radius 80%) instead of GRAPPA and Partial Fourier.

Three different k-space patterns for an acceleration factor of 7.2 were compared: $CS_{7.2,\ 80\%}$: Poisson disk radius of 80%, $CS_{7.2,\ 71\%}$: Poisson disk radius of 71% and $CS_{7.2,\ 90\%}$: Poisson disk radius of 90%.

To verify the segmentation in general, sequence $CS_{7.2,\ 80\%}$ was 3 times segmented as described before (called sequence $CS_{7.2,\ 80\%,\ 3\ Seg}$). With protocol $CS_{7.2,\ 80\%,\ 3\ Seg,\ TR2\ <\ TR1}$ the mean $\overline{TR}$ of $CS_{7.2,\ 80\%,\ 3\ Seg}$ is shortened, so that segmentation is used for acceleration.

All acquisitions have the same TE = 5.61 ms (opposed phase), readout bandwidth = 118 Hz/Px, flip angle of the saturation pulse = 90°. The differences in the protocols, regarding to the average $\overline{TR}$, mean flip angle of excitation, acceleration technique and factor, total radius of the under sampled k-space pattern, number of segments and the acquisition times, are shown in Table 1.

2.2. Reconstruction

The images were reconstructed by a nonlinear iterative SENSE type reconstruction algorithm with coil sensitivity maps for calibration consistency [32,35]. Sparsity was enforced using the L1-norm of the redundant Haar wavelet coefficient [35,38] and the following optimization problem results as described by [35]:

$$\hat{f} = argmin_f \frac{1}{2} \sum_{n=1}^{N} \|G_n - F_u(S_n \odot f)\|_2^2 + \|R \odot (Wf)\|_1 \quad (2)$$

With G_n the measured k-space data, F_u the under-sampled measurement matrix, S_n the coil sensitivity, W the redundant Haar wavelet transform, the regularization weighting factor R and f the estimated image. This minimization problem was solved by a Modified Fast Iterative Shrinkage-Thresholding Algorithm (mFISTA) [35] in 24 iterations (fixed for all reconstructions) using a modification of a Nesterov-type algorithm [35,39]. As also used in [35] a Dykstra-type algorithm [40] was utilized to efficiently solve the proximal operator. Thereby, the iterative reconstruction was not only regularized in the phase encoding and partition direction but also in readout direction (coupled reconstruction). The regularization factor R was varied for sequence $CS_{7.2,\ 80\%}$ as follows: $R = 0.01$, $R = 0.005$, $R = 0.001$, $R = 0.0005$, $R = 0.0001$, $R = 0.00005$. For all other protocols R was fixed to 0.001.

The whole reconstruction was implemented online within the manufacturer's reconstruction framework. The coil sensitivity maps are always calculated on all CPUs (Intel E5–2698 v3; 2 × 16 cores, 2.3 GHz, 256 GB RAM) in parallel, whereas the image reconstruction can be processed on the CPUs or on a GPU (Nvidia Tesla M60; 930 MHz, 16 GB RAM). On GPU the reconstruction, for the optimized sequence presented here, takes approximately 10 min.

2.3. Analyzing the data

All data were quantitatively analyzed with regard to the total number of detected vessels. The LSA were examined qualitatively and quantitatively in a volume of interest (VOI). In addition the arterial vessel-to-background ratios (aVBR) were evaluated for the different k-space sampling patterns and the venous vessel-to-background ratios (vVBR) were calculated for the segmented sequences.

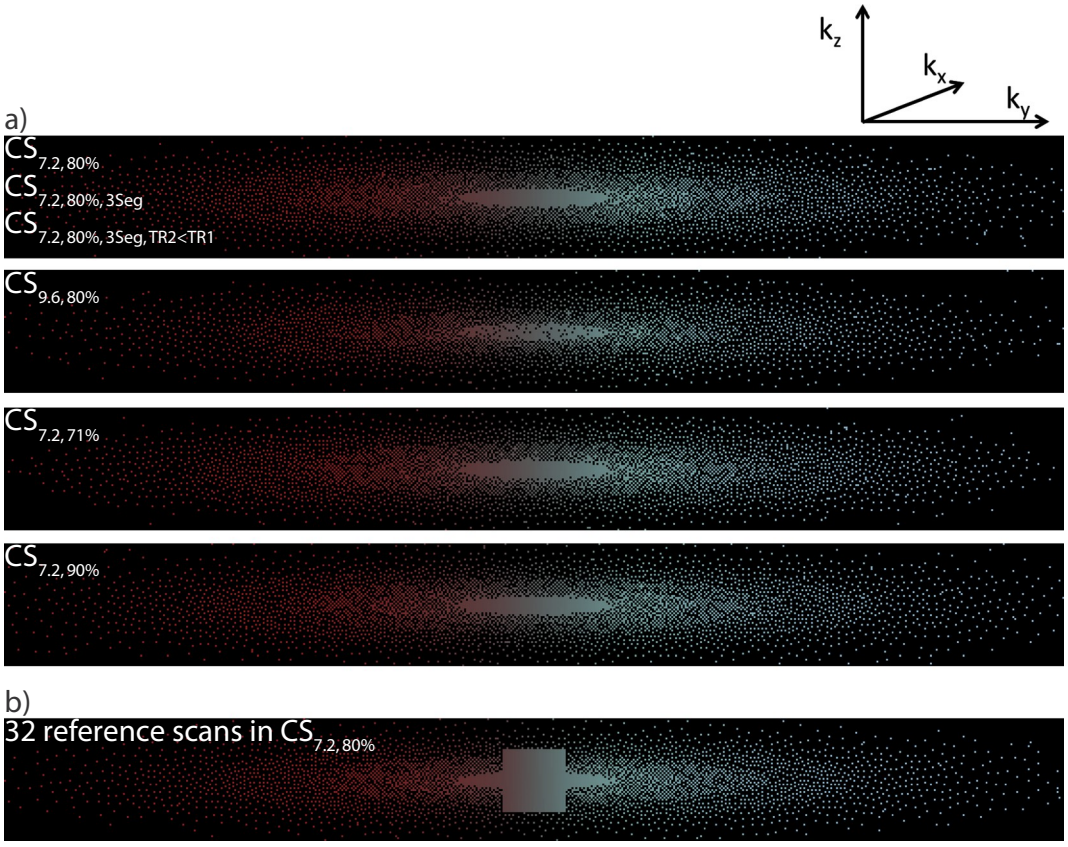

Fig. 2. Applied sampling patterns with linear reordering from red over gray to blue in the phase encoding plane (k_z: head-feet, k_y: left-right). The frequency encoding (k_x: anterior-posterior) direction is fully sampled and goes into the plane. a) Different sampling patterns of all CS sequences. The higher the acceleration, $CS_{9.6,\ 80\%}$ compared to $CS_{7.2,\ 80\%}$, $CS_{7.2,\ 80\%,\ 3\ Seg}$, $CS_{7.2,\ 80\%,\ 3\ Seg,\ TR2\ <\ TR1}$; the k-space pattern gets less dense, especially in the center. With the same acceleration but different total radius of the Poisson disc, $CS_{7.2,\ 71\%}$ and $CS_{7.2,\ 90\%}$ compared to $CS_{7.2,\ 80\%}$, $CS_{7.2,\ 80\%,\ 3\ Seg}$, $CS_{7.2,\ 80\%,\ 3\ Seg,\ TR2\ <\ TR1}$, the outer k-space is sampled more ($CS_{7.2,\ 71\%}$)/less ($CS_{7.2,\ 90\%}$) densely while the inner k-space density increases ($CS_{7.2,\ 71\%}$)/decreases ($CS_{7.2,\ 90\%}$). b) k-space pattern with 32 reference scans used for auto-calibration. The reference scans are included in all acquisitions but, to improve clarity, they have been omitted from the illustrations in a). (For interpretation of the references to colour in this figure legend, the reader is referred to the web version of this article.)

2.3.1. Quantification for total number of vessels

To determine changes in the number of detected vessels, all TOF-MRA data sets were co-registered to the conventionally accelerated sequence (Conv) which refers as gold standard in this work. Out of those, 40 mm thick, transverse maximum intensity projections (MIPs) were created (Syngo MR E11). A total number of 100 cross-sections of the MIPs were taken, which are arranged around the center line of the MIP up to ± 25% in 0.5% steps (Fig. 3). Then the maxima in the profiles of the cross-sections were counted with a minimum peak prominence of 30 (MathWorks, Matlab R2017b), which means only peaks with a relative importance of an intrinsic signal of 30 or higher are detected (compare Fig. 3 right side: the detected peaks are marked with an orange cross). This was done for any sequence in this work, as well as for the respective co-registered MIP of Conv. The total number of peaks of a sequence and the total number of peaks of Conv were compared and a relative ratio was calculated. This corresponds to the relative number of vessels of a measurement in relation to sequence Conv. Before the analyses, the skull bone including subcutaneous fat was cut off by image processing (ImageJ 1.48v) in order to prevent the detection of fat tissue or noise in the outer area as vessels.

Table 1
Parameters of the different pulse sequences: The order of the measurements was changed for each subject to exclude correlations. All sequences have a resolution of $(0.31\ mm)^3$ with a field of view (FOV) of 220x174x59 mm^3 and a distance factor of −19.64% at 4 slabs à 56 slices with 14.3% oversampling in slice direction. In sequence ($CS_{7.2,\ 80\%}$) the effect of regularization with R = 0.01, R = 0.005, R = 0.001, R = 0.0005, R = 0.0001 and R = 0.00005 was tested. All other CS-sequences are reconstructed with $R = 0.001$. The radius of the Poisson disk is defined as the relative length of the diagonal in the phase encoding plane.

Sequence	$\overline{TR}$ [ms]	TE [ms]	mean Flip angle [°]	Acceleration	Poisson disk radius [%]	No. of Segments	TA [min:ss]
Conv	23	5,61	20	GRAPPA PAT 3, Partial Fourier 6/8 (phase & slice encoding)	–	1	13:41
$CS_{9.6,\ 80\%}$	23	5,61	20	CS PAT 9.6	80	1	5:54
$CS_{7.2,\ 80\%}$	23	5,61	20	CS PAT 7.2	80	1	7:49
$CS_{7.2,\ 71\%}$	23	5,61	20	CS PAT 7.2	71	1	7:49
$CS_{7.2,\ 90\%}$	23	5,61	20	CS PAT 7.2	90	1	7:49
$CS_{7.2,\ 80\%,\ 3\ Seg}$	23	5,61	20	CS PAT 7.2	80	3	7:49
$CS_{7.2,\ 80\%,\ 3\ Seg,\ TR2\ <\ TR1}$	16.67	5,61	22	CS PAT 7.2	80	3	5:43

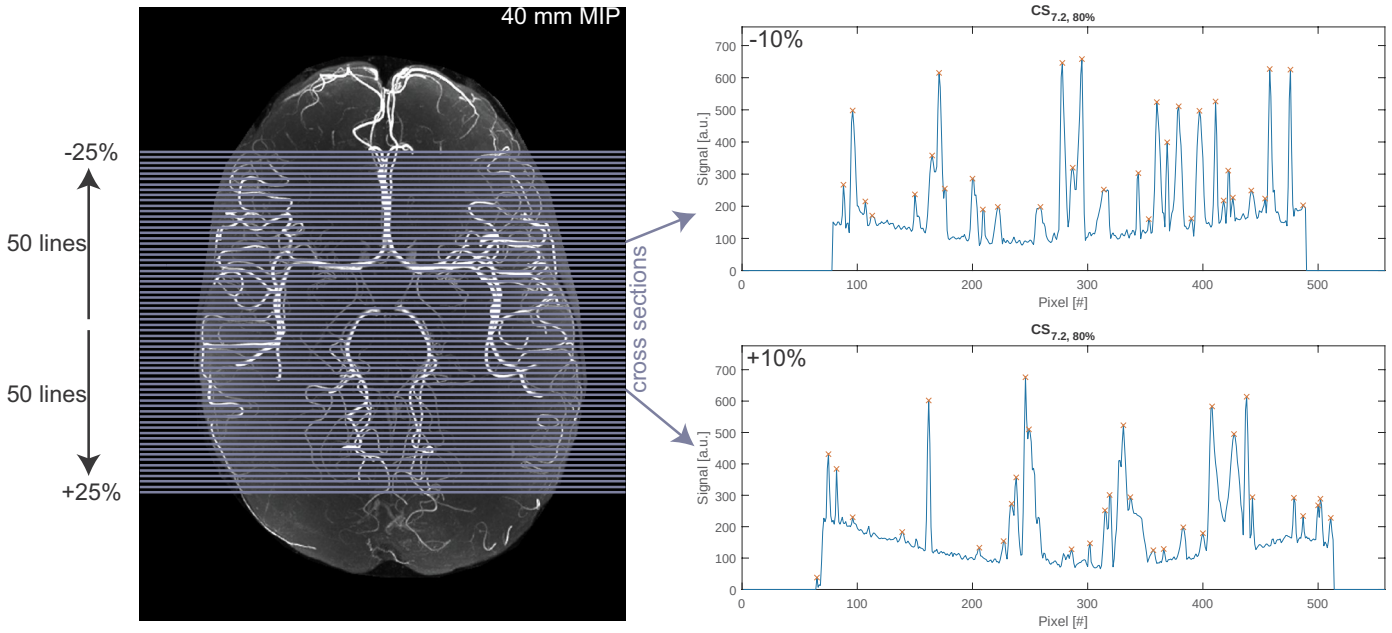

Fig. 3. Quantitative analyzes of the images exemplarily shown for sequence $CS_{7.2,\ 80\%}$. Left: Sketched drawing of the 100 cross sections of a 40 mm MIP to count the number of blood vessels. Right: Resulting cross sections at 2 of 100 positions (± 10%) of the MIP with the found peaks with a prominence of 30 (marked with an orange cross).

2.3.2. Investigation of LSA

To evaluate the performance for imaging of small vessels, the LSA were analyzed. Two radiologists (M.Sch., M.Sa.) rated coronal MIPs of the LSA (as shown in Fig. 4a) with regard to overall quality and distinctness (scale from 1 = very good to 5 = very poor). In addition, quantitative analysis was performed via multiscale vessel enhancement filtering as described by Frangi et al. [41] (Math Works, Matlab R2017b) and Fiji ImageJ (based on ImageJ 1.52n) as used in [2,42] in a VOI in co-registered images (compare Fig. 4). The parameter of the filter were optimized for small vessels: Gaussian kernel $\sigma = 0.8$, thresholds to control sensitivity $\alpha = 0.4$, $\beta = 0.3$ (compare [43]) and $c = 40$. Afterwards, in the filtered images a VOI around the LSA was defined. Following, the VOIs of the filtered images were processed via

(1) Thresholding on a 8-bit image with a lower bound value of 4 to detect vessels while background is suppressed
(2) Objects with a minimum size of 100 voxels were counted with the 3D Objects Counter
(3) Finally, the images were skeletonized and the number of branches and the total branch length were determined

2.3.3. Analysis of the contrast with regard to different CS sampling patterns

To better analyze the image contrast as a function of the k-space sampling pattern, the aVBR was calculated for three vessels (internal carotic artery, medial occipital artery and pericallosal artery). Therefore, the average signal in two regions of interests was divided, one placed in one of the arteries and one in the static background tissue. Subsequently, the resulting aVBRs per volunteer were calculated. Three sampling pattern were compared (sequences $CS_{7.2,\ 80\%}$, $CS_{7.2,\ 71\%}$ and $CS_{7.2,\ 90\%}$).

2.3.4. Investigation of the venous suppression with segmented saturation

To analyze the quality of the venous suppression, especially with sparse saturation pulses, the vVBR was calculated in all volunteers for sequence Conv, $CS_{7.2,\ 80\%}$, $CS_{7.2,\ 80\%,\ 3\ Seg}$ and $CS_{7.2,\ 80\%,\ 3\ Seg,\ TR2 < TR1}$. To calculate the vVBRs, the average signal in a region of interest in the superior sagittal sinus as well as in the sinus rectus were divided by the average signal in a region of interest in the static background tissue next to the venous vessel (compare Fig. 10 for the vVBR in the superior sagittal sinus; aVBR was calculated similarly).

For all comparisons, statistical significance was tested by pairwise *t*-test with a *p*-value below 0.05 considered as statistically significant.

3. Results

3.1. Analysis of the acceleration with CS

3.1.1. Evaluation of the acceleration factor of CS

Fig. 5 exemplarily shows the influence of sub-sampling the phase encoding in the k-space. Compared to CS (sequences $CS_{9.6,\ 80\%}$, and $CS_{7.2,\ 80\%}$), the conventional acceleration with GRAPPA PAT 3 and Partial Fourier 6/8 (slice and phase) is shown (Conv). High under-sampling results in aliasing artifacts in $CS_{9.6,\ 80\%}$, (see red arrow in Fig. 5). Moderate under-sampling in $CS_{7.2,\ 80\%}$ yields similar image quality as the conventional accelerated sequence Conv. Additionally; the CS images show reduced pulsation artifacts (see red ellipses in Fig. 5).

The quantitative analyses (Fig. 6) show that acceleration with CS ($CS_{9.6,\ 80\%}$, $CS_{7.2,\ 80\%}$) increases the total number of detected vessels significantly ($p = 0.0017$ for $CS_{9.6,\ 80\%}$, $p = 0.0006$ for $CS_{7.2,\ 80\%}$) compared to the conventionally accelerated sequence (Fig. 6a).

However in the area of the LSA (Fig. 6b–d) the number of branches does not show a significant increase between the CS sequences and Conv. Nevertheless, the measured branch length of the LSA increases for sequence $CS_{7.2,\ 80\%}$: not significantly compared to Conv ($p = 0.0512$) but compared to $CS_{9.6,\ 80\%}$ ($p = 0.0055$). In the qualitative evaluation, $CS_{7.2,\ 80\%}$ provides better overall quality and distinctness than Conv and slightly better than $CS_{9.6,\ 80\%}$ (Fig. 6d).

The acquisition times shorten from TA_{Conv} = 13:41 min to $TA_{CS9.6,\ 80\%}$ = 5:43 min and $TA_{CS7.2,\ 80\%}$ = 7:49 min.

3.1.2. Evaluation of the regularization factor of the CS reconstruction

The regularization factor has negligible influence on the image quality of large vessels (Fig. 7). A high regularization factor leads to strong smoothing and thus leads to suppression of small vessels and therefore to a reduced number of detected vessels. On the other hand,

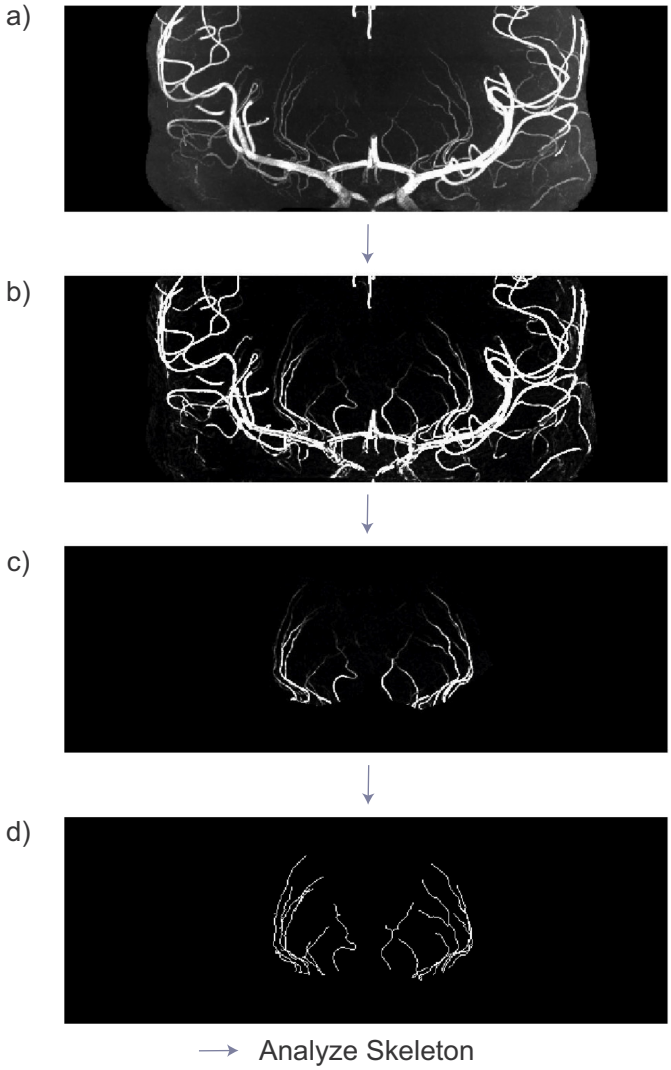

Fig. 4. Quantitative and qualitative evaluation of the LSA. The here shown images are coronal MIPs (thickness 30 mm) for better visualization. However the quantitative evaluation is done in co-registered 3D data sets. a) Example for an original image which were used for the qualitative evaluation, b) multiscale vessel enhancement filtered image, c) VOI in the filtered image, d) skeletonized image via Fiji ImageJ with finally analyzed skeleton to obtain the number of branches and the total branch length of the LSA.

for small regularization factors ($R < 0.001$), tiny vessels cannot be identified due to high noise levels (Fig. 7).

The here used quantification analysis over all slabs shows no loss of detected blood vessels for R < 0.001 (Fig. 8a), since noise is most likely detected as vessels, so the relative number of vessels saturates into a constant value. In the quantitative evaluation of the LSA (Fig. 8b, c) the number of branches increases with decreasing regularization while the branch length stays constant for $R \leq 0.001$. This leads to the hypothesis that the LSA are more fragmented with higher regularization due to noise (compare Fig. 7) and therefore the fractions are interpreted as single branches. A too high regularization ($R = 0.01$ or $R = 0.005$) leads to a reduced number of blood vessels due to smoothing, which is reflected in both metrics. The qualitative evaluations of the LSA (Fig. 8d) reflect the quantitative results and show that a regularization factor of $R = 0.001$ provides the best quality and distinctness of LSA.

3.1.3. Evaluation of the sampling pattern of CS

Beside the acceleration and regularization factor, the influence of the shape of the k-space pattern on the image quality was analyzed. Therefore, the radius of the Poisson disk was varied (Sequences $CS_{7.2,\ 80\%}$: 80%, $CS_{7.2,\ 71\%}$: 71% and $CS_{7.2,\ 90\%}$: 90%). The regularization was kept constant at the previously found R = 0.001 and the previously proven acceleration with a sub-sampling factor of 7.2 were maintained.

Regarding the total number of blood vessels (Fig. 9a), there is no significant difference between sequence $CS_{7.2,\ 80\%}$ and $CS_{7.2,\ 71\%}$ ($p = 0.0533$) as well as between $CS_{7.2,\ 80\%}$ and $CS_{7.2,\ 90\%}$ ($p = 0.6566$) whereas a significantly higher number of vessels was detected in sequence $CS_{7.2,\ 71\%}$ compared to sequence $CS_{7.2,\ 90\%}$ ($p = 0.0205$).

For the evaluated sequence patterns, the analysis of the LSA shows no differences with respect to the number of vessels (Fig. 9b) and branch length (Fig. 9c). Compared to Conv there is no increase in the numbers of branches, while the detected branch lengths of the LSA are larger for CS accelerated sequences (Fig. 9c). This is matching the qualitative interpretations as seen in Fig. 9e where all CS sampling patterns outperform Conv.

The aVBR also shows that a denser sampled k-space center does not provide a better contrast (Fig. 9d). However, the contrast with Compressed Sensing is significantly higher ($p = 1{\cdot}10^{-8}$ for $CS_{7.2,\ 80\%}$, $p = 3{\cdot}10^{-8}$ for $CS_{7.2,\ 71\%}$ and $p = 8{\cdot}10^{-8}$ for $CS_{7.2,\ 90\%}$) than in the GRAPPA and Partial Fourier accelerated sequence.

3.2. Analysis of the acceleration with CS and segmentation

To further accelerate image acquisition without introducing aliasing artifacts, segmentation was applied. Fig. 10 shows the superior sagittal sinus (SSS) of the sequences Conv (conventional acceleration), $CS_{7.2,\ 80\%}$ (accelerated with CS), $CS_{7.2,\ 80\%,\ 3\ Seg}$ (accelerated with CS and segmented with $TR_1 = TR_2$) and $CS_{7.2,\ 80\%,\ 3\ Seg,\ TR2 < TR1}$ (accelerated with CS and segmented with shortest $\overline{TR}$ which means $TR_2 < TR_1$). The venous vessels could be saturated sufficiently, however with higher segmentation the saturation effect decreases. Fig. 11 shows the mean vVBR of all volunteers of those sequences. Without segmentation, in sequence $CS_{7.2,\ 80\%}$, the vVBR was significantly decreased compared to the conventionally accelerated image acquisition ($p = 0.004$). Sparse application of saturation pulses in the segmented CS sequences ($CS_{7.2,\ 80\%,\ 3\ Seg}$ and $CS_{7.2,\ 80\%,\ 3\ Seg,\ TR2 < TR1}$) leads to an increase of the vVBR according to a lower number of saturation pulses (Fig. 10). Compared to the conventional accelerated sequence, sequence $CS_{7.2,\ 80\%,\ 3\ Seg}$ has a comparable vVBR with no significant ($p = 0.38$) difference. Also in sequence $CS_{7.2,\ 80\%,\ 3\ Seg,\ TR2 < TR1}$, with the shortest possible $\overline{TR}$, the vVBR shows the same level as Conv ($p = 0.62$).

Regarding to the total number of vessels, CS and segmentation accelerated images show no loss of vessels compared to the conventionally accelerated sequence Conv (Fig. 6). Even with $TR_1 = TR_2$ ($CS_{7.2,\ 80\%,\ 3\ Seg}$) significantly more vessels are detected in the images ($p = 0.0006$). Slightly less vessels are detected when shortening the acquisition time via segmentation ($CS_{7.2,\ 80\%,\ 3\ Seg,\ TR2 < TR1}$), but still without significance ($p = 0.57$) (Fig. 6).

The quantitative evaluation of the LSA confirms that there are no significant differences between sequences accelerated via CS and segmentation compared to Conv (Fig. 6b, c). The qualitative interpretations (Fig. 6d) show that the segmented sequences also have no difference in quality and distinctness of the LSA compared to Conv.

With sparse application of saturation pulses, additional to VERSE, in sequence $CS_{7.2,\ 80\%,\ 3\ Seg}$ ($TR_1 = TR_2$), SAR is reduced to 39.7 ± 3.8%. This is 25% lower compared to 64.5 ± 6.4% in sequence $CS_{7.2,\ 80\%}$ which only uses VERSE. For sequence $CS_{7.2,\ 80\%,\ 3\ Seg,\ TR2 < TR1}$, where $\overline{TR}$ is shortened, SAR increases to 54.2 ± 5.8%, but is still 10% lower than with fully applied saturation pulses.

4. Discussion

In this work, a TOF-MRA technique that combines several techniques such as VERSE pulses for saturation, Compressed Sensing with parallel imaging and segmentation was implemented on a 7 T ultra-high

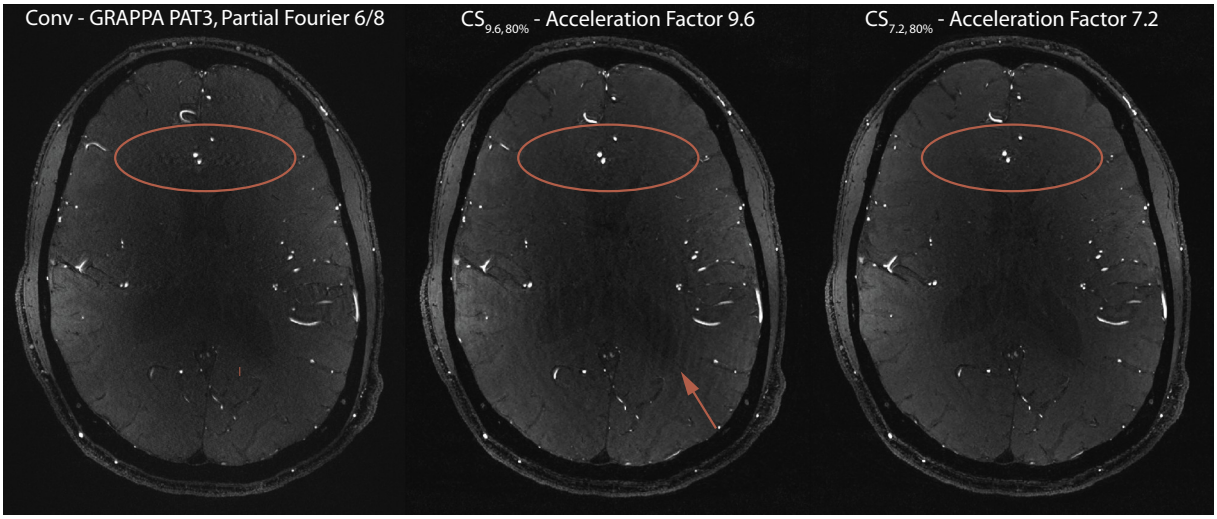

Fig. 5. Comparison between conventional acceleration with GRAPPA PAT 3 (TA = 13:41 min) and with CS with acceleration factors of 7.2 (TA = 7:49 min) and 9.6 (TA = 5:43 min): $CS_{9.6,\ 80\%}$, shows slight aliasing artifacts (red arrow), while both CS sequences show better results according to pulsation artifacts (red ellipses). (For interpretation of the references to colour in this figure legend, the reader is referred to the web version of this article.)

field MR system including online image reconstruction. To achieve a high resolution TOF-MRA protocol, the parameters were optimized in several in vivo experiments. Therefore a quantitative metric to evaluate the overall image was introduced and a metric to analyze small vessels (in this case LSA) was adapted [2] and cross-checked with a qualitative analysis by two radiologists.

In previous works, the above mentioned techniques were used only separately. In this work, the benefits of a combined application of the above mentioned techniques could be demonstrated. The acquisition time was reduced by an additional factor of 2.4 compared to the 3-fold acceleration of the conventional protocol without loss of vessels or image quality and with sufficient suppression of the venous vessels that was feasible within SAR limits. The resulting ~5 min long high resolution TOF-MRA protocol is much shorter and offers venous

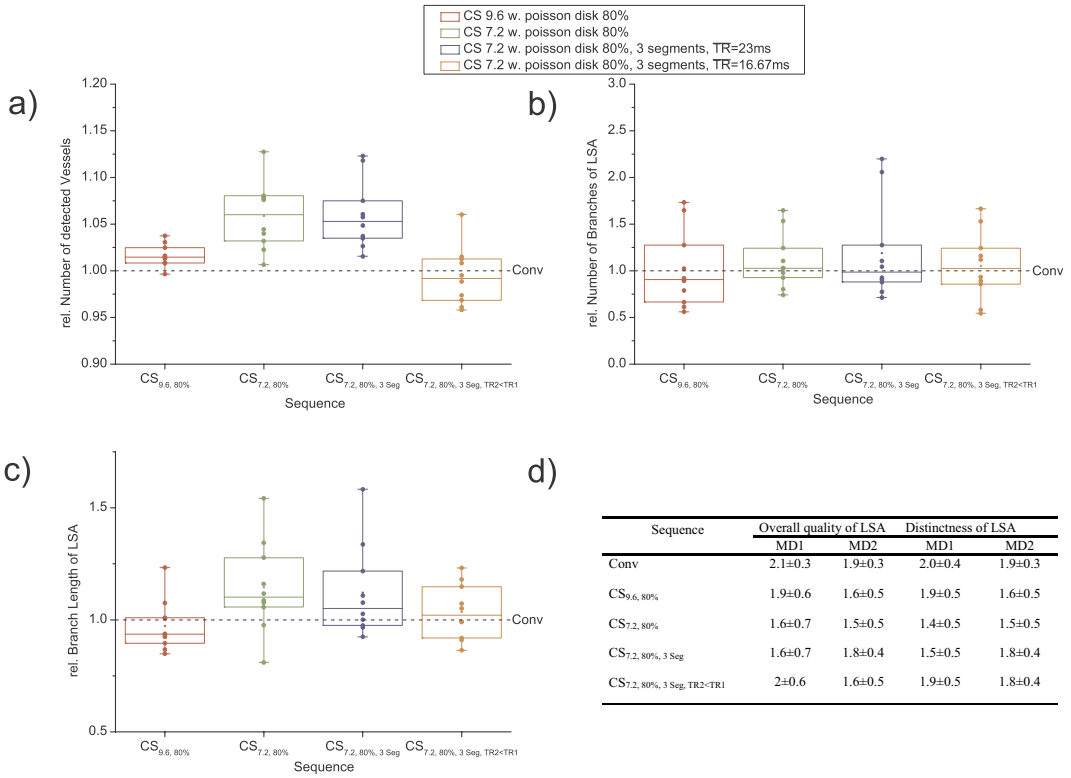

Sequence	Overall quality of LSA		Distinctness of LSA	
	MD1	MD2	MD1	MD2
Conv	2.1±0.3	1.9±0.3	2.0±0.4	1.9±0.3
$CS_{9.6,\ 80\%}$	1.9±0.6	1.6±0.5	1.9±0.5	1.6±0.5
$CS_{7.2,\ 80\%}$	1.6±0.7	1.5±0.5	1.4±0.5	1.5±0.5
$CS_{7.2,\ 80\%,\ 3\ Seg}$	1.6±0.7	1.8±0.4	1.5±0.5	1.8±0.4
$CS_{7.2,\ 80\%,\ 3\ Seg,\ TR2<TR1}$	2±0.6	1.6±0.5	1.9±0.5	1.8±0.4

Fig. 6. Number of detected vessels (a), number of branches of LSA (b), the total branch length of LSA (c) and the qualitative evaluation of the LSA (d) - all quantitative data are shown relative to the conventionally accelerated sequence Conv. a) Significantly more vessels were detected for the CS-based sequences $CS_{9.6,\ 80}$ ($p = 0.0017$), $CS_{7.2,\ 80\%}$ ($p = 0.0006$) and $CS_{7.2,\ 80\%,\ 3\ Seg}$ (p = 0.0006). The segmented CS sequence $CS_{7.2,\ 80\%,\ 3\ Seg,\ TR2\ <\ TR1}$ shows a slightly lower number of vessels but no significant difference ($p = 0.57$) to the conventionally accelerated sequence. There is no significance difference according to the number of branches (b) and branch length (c) of LSA compared to Conv. However there are significantly longer branches of LSA of $CS_{7.2,\ 80\%}$ compared to $CS_{9.6,\ 80}$ ($p = 0.0055$) Qualitatively (d) $CS_{7.2,\ 80\%}$ shows better results in both categories compared to Conv, but only slighter improvement compared to $CS_{9.6,\ 80\%}$.

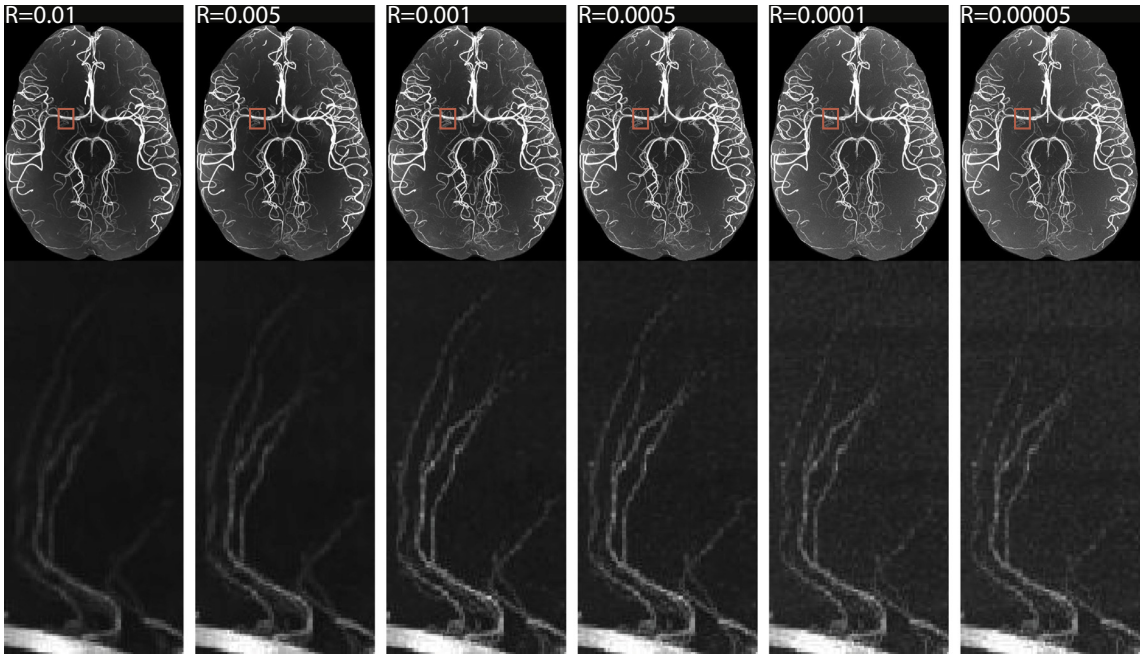

Fig. 7. Comparison of sequence $CS_{7.2,\ 80\%}$ with different regularization factors (R = 0.01, R = 0.005, R = 0.001, R = 0.0005, R = 0.0001 and R = 0.00005): If the factor is increased too much, the image is smoothed and smaller vessels are lost. If the factor is too low, the image is noisy and small vessels disappear (here zoomed to LSA, compare also the qualitative assessment of the LSA in Fig. 8d). Large vessels are generally very well represented. These analyses show that in this case R = 0.001 (compare also Fig. 8) is a good compromise between the representation of small vessels and the contrast between background and vessel.

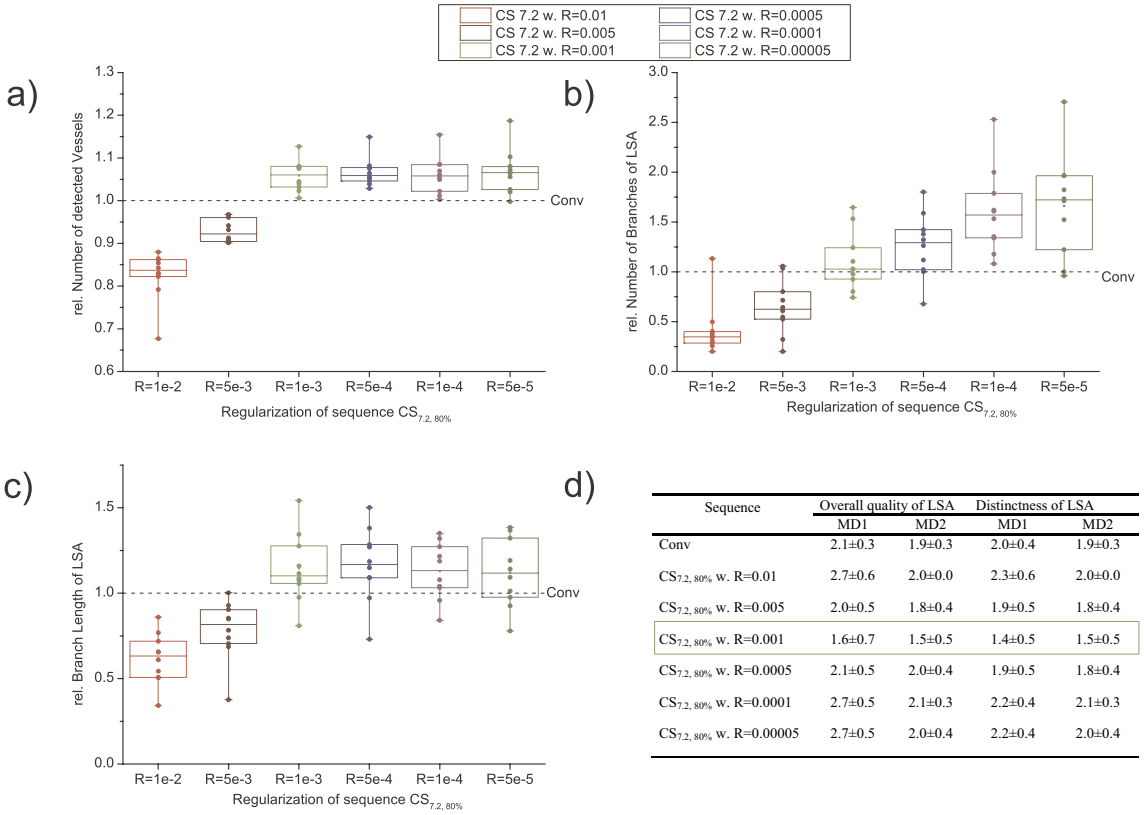

Sequence	Overall quality of LSA		Distinctness of LSA	
	MD1	MD2	MD1	MD2
Conv	2.1±0.3	1.9±0.3	2.0±0.4	1.9±0.3
$CS_{7.2,\ 80\%}$ w. R=0.01	2.7±0.6	2.0±0.0	2.3±0.6	2.0±0.0
$CS_{7.2,\ 80\%}$ w. R=0.005	2.0±0.5	1.8±0.4	1.9±0.5	1.8±0.4
$CS_{7.2,\ 80\%}$ w. R=0.001	1.6±0.7	1.5±0.5	1.4±0.5	1.5±0.5
$CS_{7.2,\ 80\%}$ w. R=0.0005	2.1±0.5	2.0±0.4	1.9±0.5	1.8±0.4
$CS_{7.2,\ 80\%}$ w. R=0.0001	2.7±0.5	2.1±0.3	2.2±0.4	2.1±0.3
$CS_{7.2,\ 80\%}$ w. R=0.00005	2.7±0.5	2.0±0.4	2.2±0.4	2.0±0.4

Fig. 8. a) Relative number of detected vessels, b), c) d) show the LSA analysis with relative number of branches of LSA (b), relative branch length of LSA (c) and the qualitative evaluation of the LSA (d) – all as a function of the regularization factors for sequence $CS_{7.2,\ 80\%}$. a) Shows for large regularization factors (R = 0.01 to R = 0.005) the relative number of detected vessels is lower than the number of vessels that were detected in the conventionally accelerated techniques. With smaller regularization (R = 0.001 to R = 0.00005), the number of detected vessels changes into a constant value. In the area of the LSA the relative number of branches continuously increases with lower regularization (b), while the branch length remains constant from R = 0.001 (c).Subfigure (d) shows that R = 0.001 has the best quality.

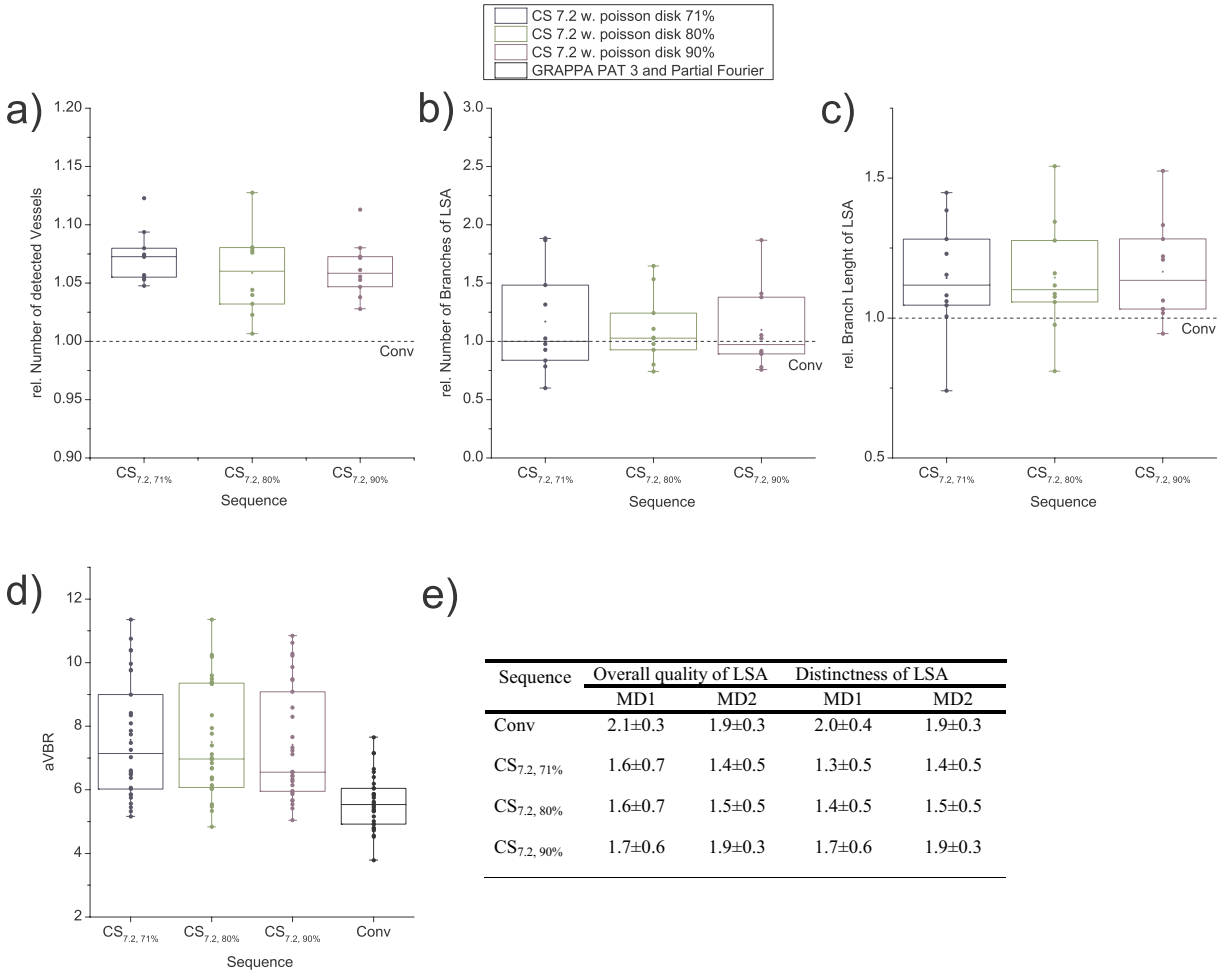

Sequence	Overall quality of LSA		Distinctness of LSA	
	MD1	MD2	MD1	MD2
Conv	2.1±0.3	1.9±0.3	2.0±0.4	1.9±0.3
$CS_{7.2,\ 71\%}$	1.6±0.7	1.4±0.5	1.3±0.5	1.4±0.5
$CS_{7.2,\ 80\%}$	1.6±0.7	1.5±0.5	1.4±0.5	1.5±0.5
$CS_{7.2,\ 90\%}$	1.7±0.6	1.9±0.3	1.7±0.6	1.9±0.3

Fig. 9. a) Relative numbers of detected vessels for the different k-space sampling patterns ($CS_{7.2,\ 80\%}$, $CS_{7.2,\ 71\%}$ and $CS_{7.2,\ 90\%}$). No significant differences ($p \geq 0.0533$) between 80% and 71% or 90% were found, but there is a significant difference between 71% and 90% ($p = 0.0205$). b) Relative number of branches of LSA without significant differences and c) relative branch length of LSA: no significant differences of CS sequences compared to Conv except for $CS_{7.2,\ 90\%}$ ($p = 0.0174$) d) Arterial vessel-to-background (aVBR). No significant differences between the different k-space sampling patterns were observed. However, the CS sequences show a significantly ($p = 1{\cdot}10^{-8}$ for $CS_{7.2,\ 80\%}$, $p = 3{\cdot}10^{-8}$ for $CS_{7.2,\ 71\%}$ and $p = 8{\cdot}10^{-8}$ for $CS_{7.2,\ 90\%}$) improved contrast compared to the conventionally accelerated sequence (Conv). e) The qualitative evaluation also shows no major differences between the quality and distinctness of the LSA in the sampling patterns of the CS accelerated sequences.

saturation as well as online reconstruction in contrast to previous works [7,8,17,20–24] to achieve acquisitions within a clinically feasible time period.

4.1. Acceleration factor

In this work, an acceleration factor of 7.2 was found to be a reasonable tradeoff between scan time and image quality, since a higher acceleration factor resulted in aliasing artifacts. The maximum intensity maps and the therein used counting of the number of vessels, as well as the evaluation of the LSA in a VOI via filtering are not influenced by the under-sampling artifacts, but for an optimized image quality aliasing is undesired. This means that there is a limit in under-sampling when using CS in TOF-MRA. This limit is higher than in previous work: 3.8 in [8] and 4 in [23] as well as in [24] where an acceleration factor of 5 was stated as the maximum for their sampling pattern to depict small vessels. At 3 T, it was stated that 6-fold acceleration should not be exceeded for the used setup [25]. However, the larger matrix sizes and the larger number of receive channel in our study compared to the 3 T study (32 vs. 20) might favor higher acceleration factors. Nevertheless, the here used acceleration factor is still much lower compared to contrast enhanced MRA (CE-MRA), where for example an acceleration factor of 30 has been applied successfully [35], which might be explained by a higher sparsity in the CE-MRA data, but, so far, CE-MRA has not yet been investigated at 7 T. For even higher spatial resolutions and corresponding larger matrix sizes the aliasing artifacts found in this work may vanish and a higher acceleration might be possible. On the other hand, larger matrix sizes lead to extended acquisition time, thus a trade-off must be found. Nonetheless, such findings also mean that CS applied to low resolution (> 0.5 mm) may offer only a limited gain in acquisition time, since these have fewer k-space lines and the acceleration is therefore limited. Additionally, with CS pulsation artifacts could be suppressed as also shown in [8]. This might be a consequence of faster acquisition and better noise reduction through regularization.

4.2. Regularization factor of the reconstruction

As it has been shown already at 3 T, the choice of the regularization factor has a strong influence on the representation of small vessels [35]. Thus, a tradeoff must be found to minimize noise and to avoid image blurring. For the applied high-resolution sequence, a regularization factor of $R = 0.001$ was considered as an optimal balance between noise and smoothing for all volunteers.

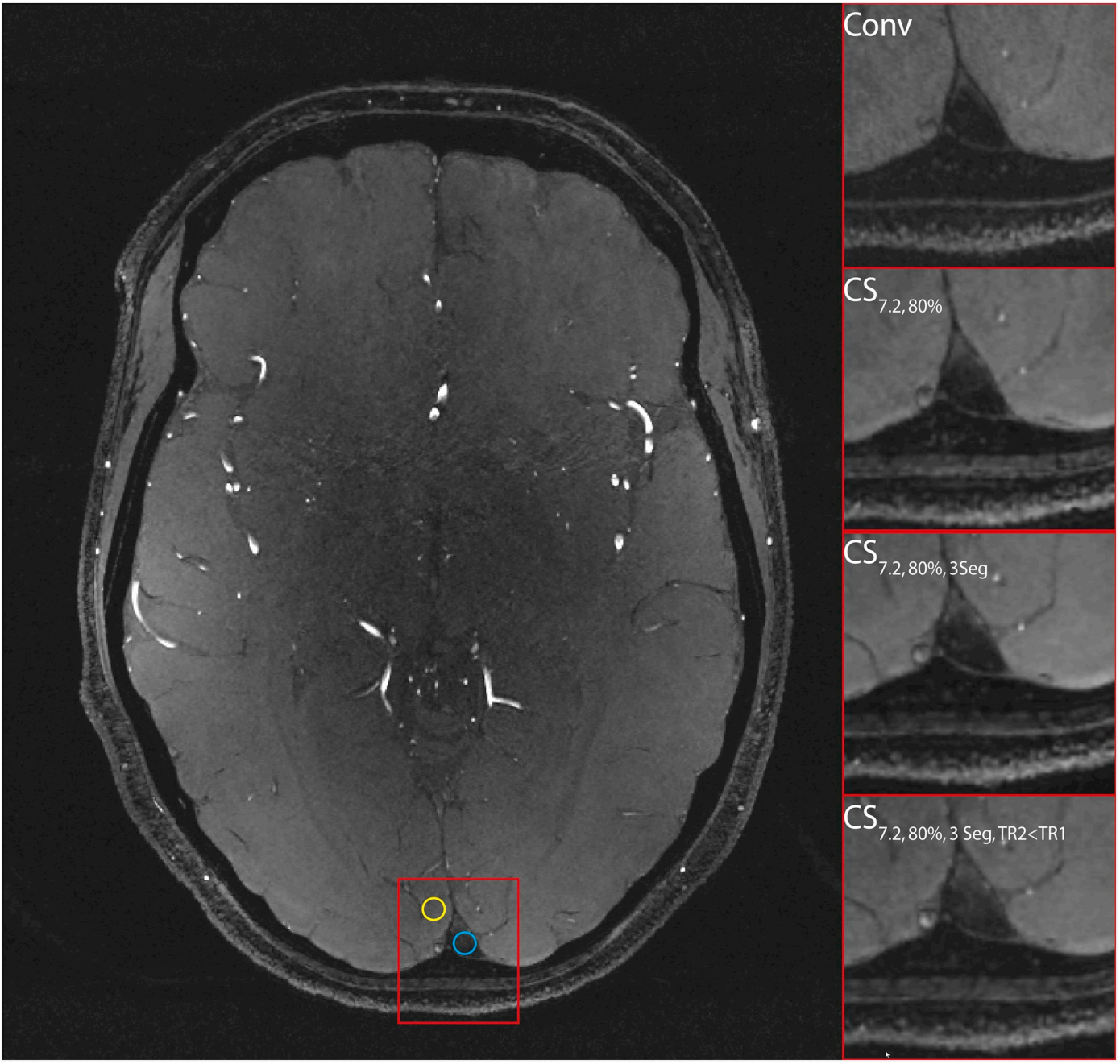

Fig. 10. Comparison of the superior sagittal sinus (SSS) of the different Sequences. The left figure shows a representative slice used to analyze the vVBR. Different regions of interest were used (blue for the signal of the SSS, yellow for the adjacent brain tissue). In the right column zoomed images of the SSS are shown (Conv, $CS_{7.2,\ 80\%}$ not segmented; $CS_{7.2,\ 80\%,\ 3\ Seg}$, $CS_{7.2,\ 80\%,\ 3\ Seg,\ TR2\ <\ TR1}$ have 3 segments). In all sequences the SSS is saturated sufficiently, but with segmentation the signal of the SSS increases compared to the acquisitions without. (For interpretation of the references to colour in this figure legend, the reader is referred to the web version of this article.)

4.3. Variation of the sampling pattern

The variation of the k-space sampling pattern did not show effects on image quality. It was expected that a larger Poisson disc radius would lead to a decreased contrast due to a lower sampling density in the k-space center while a smaller Poisson disc radius would increase the contrast but fewer vessels would be visible because of a higher subsampling in the outer k-space (compare also [24]). However, this effect was not observed. Instead a constant contrast was measured for all three radii tested and even more vessels were found in the total evaluation for a radius of 71% compared to 90%. This effect could be explained by the high contrast sensitivity of CS [30] and it shows the necessity to sample the k-space center sufficiently dense, which means in our case with a radius of at least 80%. This radius showed no difference in the number of vessels compared to the other two radii, so this size of the Poisson disc radius was chosen for further measurements. In the quantitative and qualitative evaluation of the LSA only slight differences between the sampling patterns were observed, so that also small vessels could be detected sufficiently. This is in contrast to [24], however they used a different sampling pattern than in this study. Compared to conventional acceleration, CS offered a significantly higher contrast in the aVBR. This observation agrees with Yamamoto

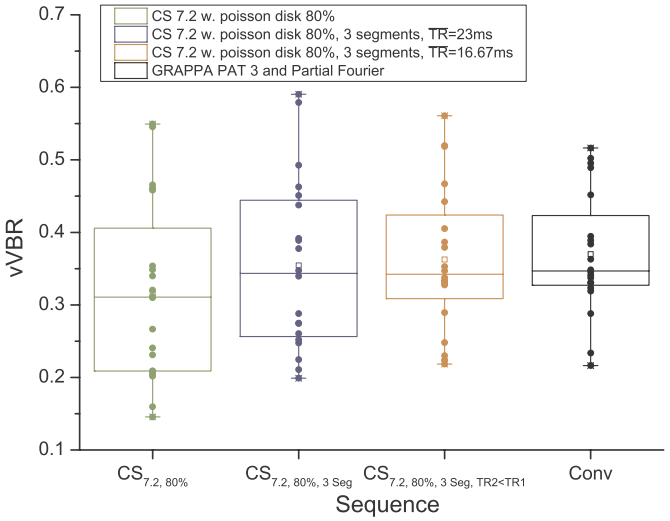

Fig. 11. Venous vessel-to-background (vVBR) of the different pulse sequences. With Compressed Sensing ($CS_{7.2,\ 80\%}$) the vVBR significantly decreases ($p = 0.004$), while with Compressed Sensing and segmentation with $TR1 = TR2$ ($CS_{7.2,\ 80\%,\ 3\ Seg}$) the vVBR increases again due to less saturation pulses. With a shortened TR ($CS_{7.2,\ 80\%,\ 3\ Seg,\ TR2 < TR1}$) the vVBR reaches the same level as the conventional accelerated sequence with no significant difference between (Conv) and ($CS_{7.2,\ 80\%,\ 3\ Seg,\ TR2 < TR1}$) ($p = 0.62$).

et al. [25] at 3 T and it could also be a consequence of the high contrast sensitivity of CS [30]. To investigate the performance of the CS sequences according to the effective resolution, the influence of the k-space pattern could be further analyzed. However, the non-stationary nature of the CS algorithms leads to a locally varying point spread function which is hard to calculate [44].

4.4. Acceleration via segmentation of the saturation pulses

With segmentation the acquisition time was additionally shortened by leaving out 66% of the VERSE venous saturation pulses. To examine the level of the venous suppression the vVBR was analyzed. The CS TOF that employs no segmentation showed lower vVBR values compared to the conventional accelerated sequence and thus yields a better venous saturation. This effect is linked to the high contrast dependence of Compressed Sensing [30]. With additional segmentation less saturation pulses are played, which leads to reduced suppression of venous vessels as seen in sequences $CS_{7.2,\ 80\%,\ 3\ Seg}$ and $CS_{7.2,\ 80\%,\ 3\ Seg,\ TR2 < TR1}$ which is also shown by [29]. However, the suppression of the venous vessels is still sufficient and comparable to the conventional accelerated sequence. Compared to previous works [29] the number of segments could be increased. For higher segmentation the vVBR increases [29] and the increased gain in time tends towards a limit per additional segment. Thus, an increase from three to four segments would only lead to a decrease in scan time of 17 s. Regarding to the total number of vessels, the number of branches in the LSA and the branch length, segmentation does not reduce the number of detected vessels compared to the conventional acceleration. However, the shortening of $\overline{TR}$ leads to a lower number of vessels compared to sequence with $TR_2 = TR_1$. That effect can be explained by the mixing of two contrasts and a consequential different saturation of small vessels. In comparison to other employed acceleration techniques, segmentation accelerates the sequence by shortening TR, due to leaving out saturation pulses, without additional under-sampling of the k-space. Further segmentation lowers SAR [29], however with VERSE saturation this is not necessarily required, but it is always desirable within UHF imaging.

4.5. CS reconstruction and reconstruction time

Image reconstruction in CS is computational-intensive and thus time-consuming. In principle, open source toolboxes such as the BART toolbox [45] could be used to reconstruct the images offline. In this work, the reconstruction is optimized for TOF-MRA and implemented in the online reconstruction system of the manufacturer [35]. Here, a reconstruction time of 2:30 min/slab (0.31 mm isotropic, matrix size of 552 × 704 × 56) was needed for the applied parameters which is considerably faster as in previous works. Natsuaki et al. [36] reported reconstruction times of 2:50 min/slab with voxel size of 0.57 × 0.57 × 1.03 mm^3 and a matrix size of 338 × 384 × 36; whereas Li et al. [46] reported 40 min/slab, a voxel size of 0.7 × 0.7 × 1.4 mm^3 and a matrix size of 256 × 256 × 48. Additionally, in this work the spatial resolution of the applied protocols is 11-times higher and the matrix size is 4.7-times larger. Furthermore, the online reconstruction offers the possibility to already start the reconstruction while scanning as long as one slab is fully acquired. This leads to an overall procedure time (acquisition and reconstruction) of maximum 12 min for all CS sequences shown here. However, reconstruction time of CS sequences is still longer than the acquisition time, which could be optimized in future work.

4.6. Limitations and outlook

This study has several limitations. At first, no fully sampled TOF-MRA was acquired for comparison. The acquisition of such a dataset requires an unacceptable long acquisition time (~1 h) - this will likely lead to motion artifacts [17] (compare supplements Sup. 3) and also it is not practical in the clinical time frame. However, the here used conventional acceleration has been reported to be sufficient for diagnosis at 1.5 and 3 T and is used in the clinical practice [47,48].

According to the two applied metrics, both have their weakness especially for low regularizations: The evaluation of the total number of vessels might misinterpret noise as vessels while the VOI metric in the LSA via filtering and ImageJ might detect too many vessels due to fragments. However, the metrics combined with the qualitative analyses show that an overall assessment as well as a small vessel assessment is possible to obtain optimized values for high resolution TOF-MRA.

An additional limitation is given by flip angle variations over the FOV due to B_1^+ inhomogeneity as a result of the shorter RF wavelength at 7 T [49,50]. This typically leads to actual flip angles that exceed the nominal flip angle in the center of the brain while they undershoot the nominal value in the outer brain regions. For TOF-MRA a higher flip angle offers higher contrast, but may saturate small vessels with low blood velocity. To control about excitation, which is subject dependent [51], parallel excitation might be employed as shown in [50].

5. Conclusion

In conclusion, the combination of VERSE for venous saturation and different acceleration techniques such as Compressed Sensing and segmentation allows the full potential of 7 T TOF-MRA to be exploited in the clinical setting. A high resolution TOF-MRA (0.31 mm isotropic) protocol that can be applied within clinically feasible acquisition times (≈5 min) was developed, which might become a new workhorse in MR-angiography imaging beyond 3/1.5 T.

Supplementary data to this article can be found online at https://doi.org/10.1016/j.mri.2019.08.014.

Declaration of competing interest

P.L., P.S., C.F. and R.M.H. are employees of Siemens Healthcare GmbH, Erlangen, Germany. A.M.N. received research support from Siemens Healthcare GmbH, Erlangen, Germany.

References

[1] Morita S, Masukawa A, Suzuki K, Hirata M, Kojima S, Ueno E. Unenhanced MR angiography: techniques and clinical applications in patients with chronic kidney disease. Radiographics 2011;31(2):E13–33. https://doi.org/10.1148/rg.312105075.

[2] Radbruch A, Eidel O, Wiestler B, Paech D, Burth S, Kickingereder P, et al. Quantification of tumor vessels in glioblastoma patients using time-of-flight angiography at 7 Tesla: a feasibility study. PLoS One 2014;9(11):e110727 https://doi.org/10.1371/journal.pone.0110727.

[3] Degnan AJ, Gallagher G, Teng Z, Lu J, Liu Q, Gillard JH. MR angiography and imaging for the evaluation of middle cerebral artery atherosclerotic disease. AJNR Am J Neuroradiol 2012;33(8):1427–35. https://doi.org/10.3174/ajnr.A2697.

[4] Deutschmann HA, Augustin M, Simbrunner J, Unger B, Schoellnast H, Fritz GA, et al. Diagnostic accuracy of 3D time-of-flight MR angiography compared with digital subtraction angiography for follow-up of coiled intracranial aneurysms: influence of aneurysm size. AJNR Am J Neuroradiol 2007;28(4):628–34.

[5] Heverhagen JT, Bourekas E, Sammet S, Knopp MV, Schmalbrock P. Time-of-flight magnetic resonance angiography at 7 Tesla. Invest Radiol 2008;43(8):568–73 https://doi.org/10.1097/RLI.0b013e31817e9b2c.

[6] Nowinski WL, Puspitasaari F, Volkau I, Marchenko Y, Knopp MV. Comparison of magnetic resonance angiography scans on 1.5, 3, and 7 Tesla units: a quantitative study of 3-dimensional cerebrovasculature. J Neuroimaging 2013;23(1):86–95. https://doi.org/10.1111/j.1552-6569.2011.00597.x.

[7] Kang CK, Park CW, Han JY, Kim SH, Park CA, Kim KN, et al. Imaging and analysis of lenticulostriate arteries using 7.0-Tesla magnetic resonance angiography. Magn Reson Med 2009;61(1):136–44 https://doi.org/10.1002/mrm.21786.

[8] Park CA, Kang D, Son YD, Kim HK, Kang CK. Microvascular imaging using compressed sensing at 7T MRI: a preliminary study. Appl Magn Reson 2015;46(11):1189–97 https://doi.org/10.1007/s00723-015-0713-0.

[9] Stamm AC, Wright CL, Knopp MV, Schmalbrock P, Heverhagen JT. Phase contrast and time-of-flight magnetic resonance angiography of the intracerebral arteries at 1.5, 3 and 7 T. Magn Reson Imaging 2013;31(4):545–9 https://doi.org/10.1016/j.mri.2012.10.023.

[10] Jellinger KA, Attems J. Prevalence and impact of cerebrovascular pathology in Alzheimer's disease and Parkinsonism. Acta Neurol Scand 2006;114(1):38–46 https://doi.org/10.1111/j.1600-0404.2006.00665.x.

[11] Minagar A, Jy W, Jimenez JJ, Alexander JS. Multiple sclerosis as a vascular disease. Neurol Res 2006;28(3):230–5 https://doi.org/10.1179/016164106X98080.

[12] Ladd Mark E, Bachert P, Meyerspeer Martin, Moser Ewald, Nagel Armin M, Norris David G, et al. Pros and cons of ultra-high-field MRI/MRS for human application. Prog Nucl Magn Reson Spectrosc 2018;109:1–50.

[13] Pohmann R, Speck O, Scheffler K. Signal-to-noise ratio and MR tissue parameters in human brain imaging at 3, 7, and 9.4 tesla using current receive coil arrays. Magn Reson Med 2016;75(2):801–9 https://doi.org/10.1002/mrm.25677.

[14] Kraff O, Fischer A, Nagel AM, Monninghoff C, Ladd ME. MRI at 7 tesla and above: demonstrated and potential capabilities. J Magn Reson Imaging 2015;41(1):13–33. https://doi.org/10.1002/Jmri.24573.

[15] Maderwald S, Ladd SC, Gizewski ER, Kraff O, Theysohn JM, Wicklow K, et al. To TOF or not to TOF: strategies for non-contrast-enhanced intracranial MRA at 7 T. Magma 2008;21(1–2):159–67 https://doi.org/10.1007/s10334-007-0096-9.

[16] Rooney WD, Johnson G, Li X, Cohen ER, Kim SG, Ugurbil K, et al. Magnetic field and tissue dependencies of human brain longitudinal 1H2O relaxation in vivo. Magn Reson Med 2007;57(2):308–18 https://doi.org/10.1002/mrm.21122.

[17] Mattern H, Sciarra A, Godenschweger F, Stucht D, Lusebrink F, Rose G, et al. Prospective motion correction enables highest resolution time-of-flight angiography at 7T. Magn Reson Med 2018;80(1):248–58 https://doi.org/10.1002/mrm.27033.

[18] Griswold MA, Jakob PM, Heidemann RM, Nittka M, Jellus V, Wang J, et al. Generalized autocalibrating partially parallel acquisitions (GRAPPA). Magn Reson Med 2002;47(6):1202–10 https://doi.org/10.1002/mrm.10171.

[19] Pruessmann KP, Weiger M, Scheidegger MB, Boesiger P. SENSE: sensitivity encoding for fast MRI. Magn Reson Med 1999;42(5):952–62.

[20] Johst S, Schmitter S, Wrede K. High-resolution clinical 7T protocol for the depiction of cerebral vascular structures. Proceedings of the 19th annual meeting of ISMRM. Montreal. 2011. p. 4243.

[21] Johst S, Wrede KH, Ladd ME, Maderwald S. Time-of-flight magnetic resonance angiography at 7 T using venous saturation pulses with reduced flip angles. Invest Radiol 2012;47(8):445–50 https://doi.org/10.1097/RLI.0b013e31824ef21f.

[22] Wrede KH, Johst S, Dammann P, Ozkan N, Monninghoff C, Kraemer M, et al. Improved cerebral time-of-flight magnetic resonance angiography at 7 Tesla—feasibility study and preliminary results using optimized venous saturation pulses. PLoS One 2014;9(9):e106697 https://doi.org/10.1371/journal.pone.0106697.

[23] Milles J, Versluis MJ, Webb AG, Reiber JHC. Quantitative evaluation of compressed sensing in MRI: application to 7T time-of-flight angiography. Proceedings of the 10th IEEE international conference on information technology and applications in biomedicine. Corfu, Greece. 2010 https://doi.org/10.1109/ITAB.2010.5687775.

[24] Kang C-K, Son Y-D, Kim H-K. Energy Spectrum-based variable-density sampling distribution optimized for MR angiography at compressed sensing technique. Appl Magn Reson 2015;47:201–10 https://doi.org/10.1007/s00723-015-0742-8.

[25] Yamamoto T, Fujimoto K, Okada T, Fushimi Y, Stalder AF, Natsuaki Y, et al. Time-of-flight magnetic resonance angiography with sparse undersampling and iterative reconstruction: comparison with conventional parallel imaging for accelerated imaging. Invest Radiol 2016;51(6):372–8 https://doi.org/10.1097/RLI.0000000000000221.

[26] Wiesinger F, Boesiger P, Pruessmann KP. Electrodynamics and ultimate SNR in parallel MR imaging. Magn Reson Med 2004;52(2):376–90 https://doi.org/10.1002/mrm.20183.

[27] Vaughan JT, Garwood M, Collins CM, Liu W, DelaBarre L, Adriany G, et al. 7T vs. 4T: RF power, homogeneity, and signal-to-noise comparison in head images. Magn Reson Med 2001;46(1):24–30.

[28] Schmitter S, Bock M, Johst S, Auerbach EJ, Ugurbil K, Van de Moortele PF. Contrast enhancement in TOF cerebral angiography at 7 T using saturation and MT pulses under SAR constraints: impact of VERSE and sparse pulses. Magn Reson Med 2012;68(1):188–97 https://doi.org/10.1002/mrm.23226.

[29] Zhang Z, Deng X, Weng D, An J, Zuo Z, Wang B, et al. Segmented TOF at 7 T MRI: technique and clinical applications. Magn Reson Imaging 2015;33(9):1043–50 https://doi.org/10.1016/j.mri.2015.07.002.

[30] Lustig M, Donoho D, Pauly JM. Sparse MRI: the application of compressed sensing for rapid MR imaging. Magn Reson Med 2007;58(6):1182–95 https://doi.org/10.1002/mrm.21391.

[31] Lustig M. L1 SPIR-iT: autocalibrating parallel imaging compressed sensing. Proceedings of the 20th annual meeting of ISMRM. 2009. p. 334. Honolulu.

[32] Uecker M, Lai P, Murphy MJ, Virtue P, Elad M, Pauly JM, et al. ESPIRiT—an eigenvalue approach to autocalibrating parallel MRI: where SENSE meets GRAPPA. Magn Reson Med 2014;71(3):990–1001 https://doi.org/10.1002/mrm.24751.

[33] Conolly S, Nishimura D, Macovski A. Variable-rate selective excitation. J Magn Reson 1988;78:440–58.

[34] IEC 60601-2-33. Medical electrical equipment - part 2–33: particular requirements for the basic safety and essential performance of magnetic resonance equipment for medical diagnosis. International Electrotechnical Commission; 2010.

[35] Stalder AF, Schmidt M, Quick HH, Schlamann M, Maderwald S, Schmitt P, et al. Highly undersampled contrast-enhanced MRA with iterative reconstruction: integration in a clinical setting. Magn Reson Med 2015;74(6):1652–60 https://doi.org/10.1002/mrm.25565.

[36] Natsuaki Y. Time-of-flight with sparse undersampling (TOFu): towards practical MR applications of the compressed sensing. Proceedings of the 22nd annual meeting of ISMRM. 2014. p. 941. Milan.

[37] Atkinson D, Brant-Zawadzki M, Gillan G, Purdy D, Laub G. Improved MR angiography: magnetization transfer suppression with variable flip angle excitation and increased resolution. Radiology 1994;190(3):890–4 https://doi.org/10.1148/radiology.190.3.8115646.

[38] Liu Jun, Rapin J, Chang Ti-chiun, Lefebvre Alban, Zenge Michael, Mueller Edgar, et al. Dynamic cardiac MRI reconstruction with weighted redundant Haar wavelets. Proceedings of the 20th annual meeting of ISMRM. 2012. p. 4249. Melbourne.

[39] Beck A, Teboulle M. A fast iterative shrinkage-thresholding algorithm for linear inverse problems. SIAM J Imag Sci 2009;2(1):183–202 https://doi.org/10.1137/080716542.

[40] Dykstra RL. An algorithm for restricted least squares regression. J Am Stat Assoc 1983;78(384):837–42 https://doi.org/10.1080/01621459.1983.10477029.

[41] Frangi AF, Niessen WJ, Vincken KL, Viergever MA. Multiscale vessel enhancement filtering. Medical Image Computing and Computer-Assisted Intervention - MICCAI. 1998. p. 130–7.

[42] Tischer C, Tosi S. Tumor blood vessels: 3D tubular network analysis. In: Miura K, editor. Bioimage data analysis. 2016. p. 219–36.

[43] Chapman BE, Parker DL. 3D multi-scale vessel enhancement filtering based on curvature measurements: application to time-of-flight MRA. Med Image Anal 2005;9(3):191–208 https://doi.org/10.1016/j.media.2004.08.001.

[44] Wech T, Stäb D, Fischer A, Hahn D, Köstler H. On the quality evaluation for images reconstructed by compressed sensing. Montreal: ISMRM; 2011.

[45] Uecker M, Ong F, Tamir J. Berkeley advanced reconstruction toolbox. Proceedings of the 23rd annual meeting of ISMRM. Toronto. 2015. p. 2486.

[46] Li B, Li H, Kong H, Dong L, Zhang J, Fang J. Compressed sensing based simultaneous black- and gray-blood carotid vessel wall MR imaging. Magn Reson Imaging 2017;38:214–23 https://doi.org/10.1016/j.mri.2017.01.013.

[47] Gaa J, Weidauer S, Requardt M, Kiefer B, Lanfermann H, Zanella FE. Comparison of intracranial 3D-ToF-MRA with and without parallel acquisition techniques at 1.5T and 3.0T: preliminary results. Acta Radiol 2004;45(3):327–32.

[48] Gizewski ER, Maderwald S, Wanke I, Goehde S, Forsting M, Ladd ME. Comparison of volume, four- and eight-channel head coils using standard and parallel imaging. Eur Radiol 2005;15(8):1555–62 https://doi.org/10.1007/s00330-005-2730-0.

[49] Padormo F, Beqiri A, Hajnal JV, Malik SJ. Parallel transmission for ultrahigh-field imaging. NMR Biomed 2016;29(9):1145–61 https://doi.org/10.1002/nbm.3313.

[50] Schmitter S, Wu X, Auerbach EJ, Adriany G, Pfeuffer J, Hamm M, et al. Seven-tesla time-of-flight angiography using a 16-channel parallel transmit system with power-constrained 3-dimensional spoke radiofrequency pulse design. Invest Radiol 2014;49(5):314–25 https://doi.org/10.1097/RLI.0000000000000033.

[51] Liu W, Collins CM, Smith MB. Calculations of B1 distribution, specific energy absorption rate, and intrinsic signal-to-noise ratio for a body-size birdcage coil loaded with different human subjects at 64 and 128 MHz. Appl Magn Reson 2005;29(1):5–18 https://doi.org/10.1007/BF031669.